

Imaging the Effect of the Intermediate Principal Stress on Strength, Deformation and Transport Properties of Rocks Using Seismic Methods

R.P. Young & M.H.B. Nasser

Lassonde Institute and Department of Civil Engineering University of Toronto, Toronto, Canada

L. Lombos

ErgoTech Ltd., Glan Conwy, Wales, UK

ABSTRACT: Our experimental investigation extends previous work to study the role of an independent σ_2 stress using enhanced geophysical imaging techniques including continuous acoustic emission (AE) recording and ultrasonic wave velocity (V_p & V_s) measurements. Our results for a $\sigma_1 > \sigma_2 > \sigma_3$ stress state, show a self-consistent relationship among strength, 3D deformation, 3D wave velocities, AE and 3D permeability (K) during the various stages of deformation in Fontainebleau sandstone. The K value reduced dramatically (50%) along all three axes when σ_1 reached the failure point at 0.5% of axial strain accompanied by a significant episode of AE activity. V_p measured parallel to the σ_1 shows a 20% increase during the test, whereas V_p measured along the σ_2 and σ_3 directions both show an initial 10% increase up to the failure point followed by a 2 and 5% decrease in the post failure regime respectively. V_s shows a 35, 17 and 5% increase along σ_1 , σ_2 and σ_3 directions up to the failure point with a small reduction of 2-3% for all three directions during post failure regime when σ_1 reached 250 MPa.

1 INTRODUCTION

1.1 *Effect of intermediate principal stress*

Fracturing contributes to seismic behavior, mechanical properties and rock fluid interactions and is important in the understanding of natural geologic hazards such as volcanic activity and earthquakes and engineering applications such as mining, hydrocarbon recovery, the management of groundwater and deep underground storage for nuclear waste isolation and CO₂ sequestration. To enhance the understanding of how different rock types fracture, induce seismicity, change elastic properties and transport fluids under three-dimensional compressive stress regimes, a state of the art true triaxial geophysical imaging cell is used at the Rock Fracture Dynamic Facility (RDFD).

The influence of intermediate principal stress on the behaviour and mechanical properties of rocks is now widely acknowledged. Perhaps the greatest contribution to the study of brittle fracture and its dependence on the intermediate principal stress was made by Mogi (1967, 1971). He designed and utilized a high-pressure true triaxial stress apparatus for testing hard rocks under three independently applied principal stresses. Takahashi and Koide (1989) designed and fabricated a near replica of Mogi's (1971) true triaxial cell to accommodate larger specimens for testing rocks such as sandstones and shales. Haimson and Chang (2000) also designed and fabricated a true triaxial testing system and determined that, dilatancy is more pronounced at low intermediate stress magnitudes but diminishes at higher levels, supporting the result obtained by Takahashi and Koide (1989). It became further evident that at higher intermediate stress levels, the elastic range of the stress-strain behaviour of rocks for a given minimum stress gets extended. The evolution of such true-triaxial testing systems (Descamps and Tshibangu, 2007) led to improvement of the original true-triaxial strength criteria (You, 2009) as suggested by Mogi (1971). This criteria were applied to in-situ situations to predict the failure strength of rocks at depth where larger intermediate principal stresses prevailed, such as in the San Andreas Fault Observatory as well as in the US and Taiwan Chelungpu-fault Drilling Projects (Haimson, 2006, Haimson et al., 2010). King (2002) and King et al. (2011) developed a true-triaxial loading system for introducing multiple parallel fractures in cubic specimens of low strength sedi-

mentary rocks and for determining elastic properties, sonic wave velocities and acoustic emission associated with the formation of fracture sets in sandstone under polyaxial stress conditions. In addition, advanced numerical methods have enhanced the analysis of geometrically complex geological and geotechnical problems during the last decade. Cai (2007) used an FEM/DEM combined numerical tool to investigate the impact of intermediate stress on rock fracturing and strength near excavation boundaries concluding that the generation of tunnel surface parallel fractures (onion skins, spalling and slabbing) is attributed to the existence of moderate intermediate principal stress and low to zero minimum confinement. He emphasized that further experimental and numerical study is needed to investigate the full impact of intermediate stress on the strength and behavior of rock.

The mechanical and transport properties of crustal rocks are profoundly influenced by cracks and pore spaces. The existence of embedded microcrack fabrics in rocks significantly influences the elastic moduli, seismic wave velocities and inferred permeability as shown by Heard and Page (1982), Guéguen and Dienes (1988), Guéguen et al. (2003), Reuschle et al. (2006), Schubnel et al. (2003 and 2006), Nasseri et al. (2009). Song and Renner (2007) studied the hydromechanical properties of Fontainebleau sandstone by measuring ultrasonic velocity, hydraulic permeability and specific storage capacity of eight blocks covering a range of connected porosity from 3% to 10%. The permeability of tested samples varied from $10E-13$ m² down to $10E-20$ m² depending primarily on their porosity and pore geometry. However most of these studies were carried out under hydrostatic or deviatoric stress induced damage due to the nucleation and propagation of microcracks in specimens in which the intermediate and minimum stresses were equal. The present research will extend these investigations to study the role of an independent intermediate principal stress using enhanced geophysical imaging techniques to understand induced damage and its effect on the 3D transport properties of Fontainebleau sandstone.

1.2 Rock Fracture Dynamic Facility (RFDF)

An integrated rock testing facility (Fig. 1) with geophysical monitoring, real time results visualization and numerical modelling capabilities have been developed to address critical gaps in the science of rock fracture and enable new discoveries. The polyaxial loading frame with an integral geophysical imaging cell has capabilities that are unique.

The following are some of the specifications of the RFDF:

- A polyaxial servo-controlled rock deformation system allowing 6800 kN of axial force and 3400 kN of lateral force,
- Polyaxial geophysical imaging cell (GICB),
- 18 Acoustic Emission sensors (dual mode receiver and pulser),
- Dedicated P, S1, S2 velocity measurements in three orthogonal axes, (X, Y and Z),
- Temperature up to 200°C, stress and strain recording (total of nine LVDT along three axes),
- Full waveform continuous Acoustic Emission monitoring at 10 MHz sampling rate for a period of 8 hours for 18 channels,
- Permeability and pore pressure measuring system along three axes,
- A 256 processor (64 node) parallel computer cluster for modelling and real time data analysis.

2 EXPERIMENTAL SET UP AND TESTING PROCEDURE

2.1 Sample preparation for true triaxial experiment

A Fontainebleau sandstone cube of 8 cm³ dimension was cut from a larger block. Using a Wasino CNC grinding machine, the larger cube was reduced to 8 cm³ with an accuracy of 5 micron flatness on each face. A systematic machining methodology was adopted to guarantee parallelism of opposite faces to within 5 microns. The grinding program was set to shave 100 microns on each lap with a much finer and slower rate on final polishing laps. A special vise and machining methodology was adopted to chamfer all edges of the specimen to a final width of 4 mm as required for edge-sealing purposes. Fontainebleau cubical specimens were oven-dried at a temperature of 70°C for a period of 24 hours followed by 24 hours of vacuum induced saturation.

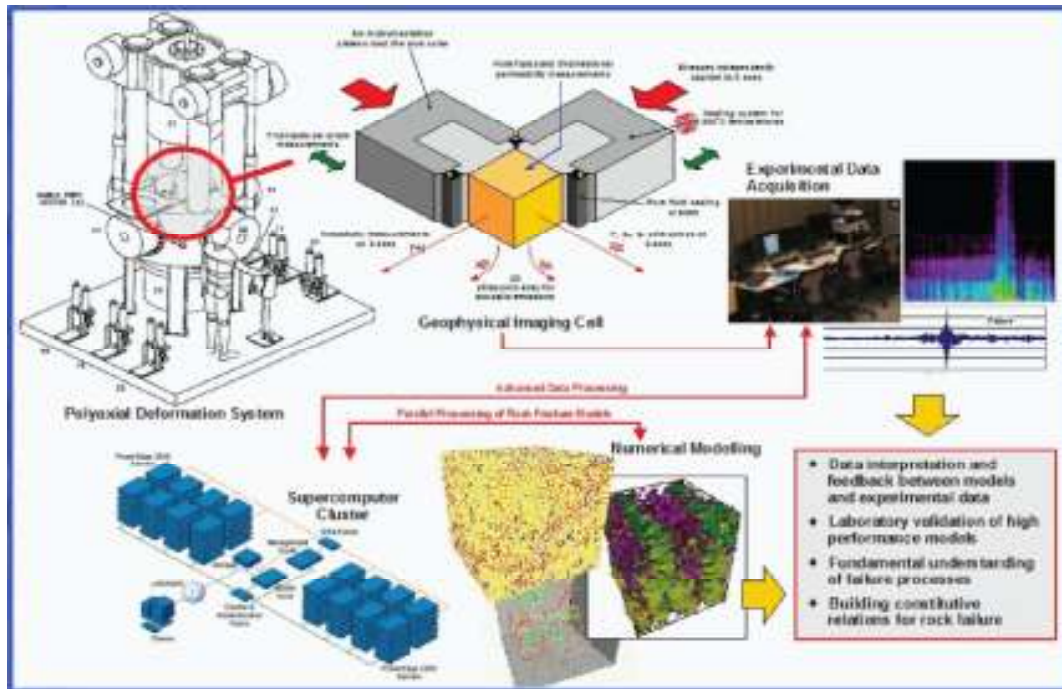


Figure 1. Shows the overall components and concepts for true triaxial geophysical imaging cell, loading machine and numerical modelling capabilities at RFDf.

Measurements of dry and saturated mass and volume were used to calculate the specimen's porosity (~5%) dry density (2.47 g/cc) and saturated density (2.49g/cc). Fontainebleau sandstone is a quartz arenite of Oligocene age collected in the France region around Paris (Haddad et al., 2006). Fredrich et al. (1993) characterized the pore geometry of four samples of Fontainebleau sandstone using laser scanning confocal microscopy with their effective porosities ranged from 4% to 20%.

The experiment was performed using a unique true triaxial geophysical imaging cell within a custom made MTS polyaxial loading frame. First the specimen was loaded hydrostatically at 0.0002 mm/s up to 5 and 10 MPa of effective stress respectively. Ultrasonic wave velocity measurements were simultaneously measured at every 1-2 MPa of loading along all three axes (one vertical and two horizontal directions). Acoustic emissions (triggered data catalogue) and a continuous wave form streaming system were armed to record events on all 16 channels. At 5 MPa of hydrostatic stress Flexible Rubber Membrane (Fig. 2) was activated by applying 2 MPa seal pressure to all 12 edges of the Cubic Skeleton Rubber Seal–Mickey Mouse (MM seal) enclosing the cubic specimen followed by directional permeability measurements based on steady-state flow method.

The experiment was carried out under drained conditions with the down stream flow exposed to atmospheric pressure. At 10 MPa of hydrostatic stress directional permeability measurements were repeated along the three principal stress axes. At this point keeping σ_3 at 10 MPa, σ_2 and σ_3 were raised simultaneously under drained conditions to 20 MPa of stress. 3D permeability and 3D ultrasonic wave velocity were measured systematically. Next σ_1 was increased with the same displacement rate along the main principal stress direction (vertical axis) until failure and beyond. Acoustic emission, wave velocity tomography, 3D stress-strain and 3D directional permeability were monitored according to the pre-designed testing plan at various stress increments of σ_1 .

2.2 True triaxial geophysical imaging cell (TTGIC)

Figure 2 shows the plane view of the cell with a description of its components. Activation of the MM seal isolated all faces of the cubical specimen to facilitate measurements of the transport properties independently along each principal stress axis. Nine LVDTs (three along each axis) are used to measure the deformation of the rock independently along each principal stress axis.

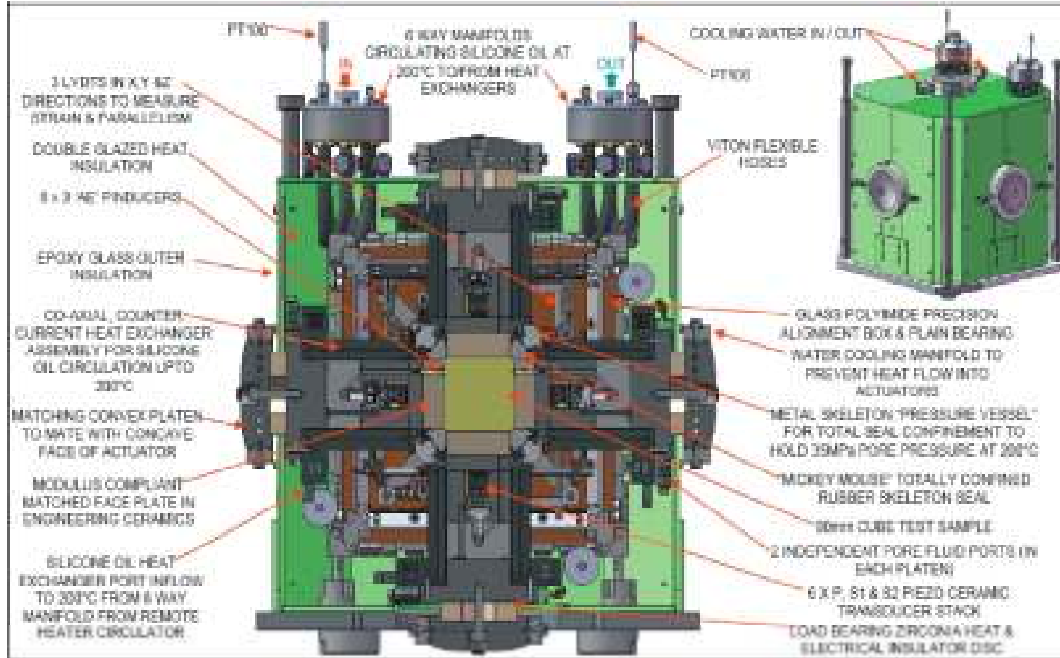


Figure 2. Shows detailed components of TTGIC designed and manufactured by ErgoTech.

Two independent pore fluid ports at the surface of each platen deliver fluid and measure pore pressure independently along each principal stress axis. The face of each loading platen (six platens) contains three dual mode AE pinducers with a resonant frequency of 1.3 MHz. In addition each loading platens has P, S₁ and S₂ piezo ceramic (800 kHz resonant frequency) transducers embedded within the platen. Detail of the design and development of the integrated true triaxial geophysical imaging cell is discussed in the paper by Lombos et al. (2011) at the same international ISRM workshop on true triaxial testing of rocks.

2.3 MTS polyaxial testing machine

The experimental setup includes a custom made polyaxial servo-controlled MTS rock deformation system to load cubic rock specimens placed within the geophysical imaging cell. This testing frame uses a swing arm to place the TTGIC into the polyaxial loading frame using a moveable cross head. The MTS polyaxial testing machine can deliver an axial stress of ~1 GPa in the σ_1 axis and ~500 MPa of lateral stress in the horizontal axes of σ_2 and σ_3 . Six loading actuators can be controlled in pair under compressional and translational mode independently. Multipurpose Test Ware software (979) is used for controlling the loading system.

2.4 Permeability and rubber membrane skeleton - MM seal pressure system

Figure 3 shows the experimental set up used to measure directional permeability along all three principal stress axes using the steady-state method. A servo-controlled Isco-Teledyne system was used to pump silicone oil into one side of a moving diaphragm at various flow rates in ranging from 0.001 to 25 ml/min. The Isco-Teledyne system can be set to work in either constant flow rate or constant pressure mode. Distilled, de-aired water is pushed from the other side of

the liquid-liquid interface into a manifold and is then directed independently into each upstream platen using six controlling valves. The fluid passes through the specimen and exits via downstream platen after which it passes through a filter and returns to the reservoir as shown in Figure 3. Six pore pressure transducers mounted on each loading platens (upstream and downstream sides, Fig. 4a) measure the pore pressure differences as a function of various constant flow rates controlled by the Isco-Teledyne pump system. A Quizix pump is used in combination with a smaller capacity liquid-liquid interface moving diaphragm which has been set up in reverse of the first system. The Quizix pump pressurizes the water on the inlet side of the said diaphragm under constant pressure mode and pushes silicone oil out to pressurize the MM seal when inflatable flexible membrane along twelve edges of 8 cm³ specimen is activated (Fig. 4b). A Labview program is used to plot real time effective stress and strain along three principal stress axes and the directional permeability based on set flow rates (Q in ml/s) which causes pore pressure differences (d_p in Pa). A diagnostic real time plot was developed to monitor the variation between Q and d_p once stable pore pressures is established across opposite faces (upstream and downstream sides) of the cube. Points are added (3-4 points) for various flow rates and if a straight line is formed between these points, then Darcy's Law is satisfied and laminar flow is present along each axis. The directional permeability (K in m²) is calculated instantaneously using the aforementioned program. Variation of pore pressure measured at each individual face of the sample during directional permeability measurements is logged for further cross checking with the instantaneous permeability values.

2.5 Ultrasonic wave velocity and acoustic emission

16 piezoelectric pinducers with a 1.3 MHz resonant frequency are in direct contact with the cubic sample. Each of these pinducers can be used as a passive or active source for determining wave velocity evolution during the experiment. Output signals were sampled at 10 MHz and were recorded in two AE catalogues. Transducers signals were amplified by 40 dB.

Firstly, discrete AE events were recorded throughout the experiment if the amplitude in four or more channels exceeded a 40 mV threshold. Triggered AE waveform data were recorded with each event having a trace length of 204.8 μ s at a maximum capacity of 60 events per second. The number of times events are triggered was recorded as well (THC). Secondly, full wave form data was recorded using the Richter System (ASC) which has a 12-bit data acquisition card directly linked to hard drive of eight streaming units (two channels per unit) each of which has ~one TB of storage capacity. This unique capability allows 6-8 hours of continuous recording at 10 MHz of sampling rate. The full-wave form triggering process and wave analysis is carried out with ASC's InSite seismic processing software.

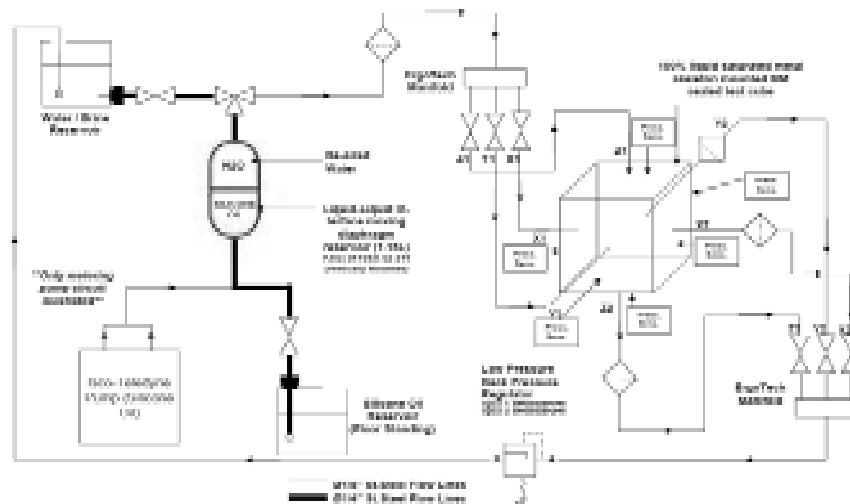


Figure 3. Experimental set up to measure directional steady-state permeability at RFDF, designed and drawn by ErgoTech.

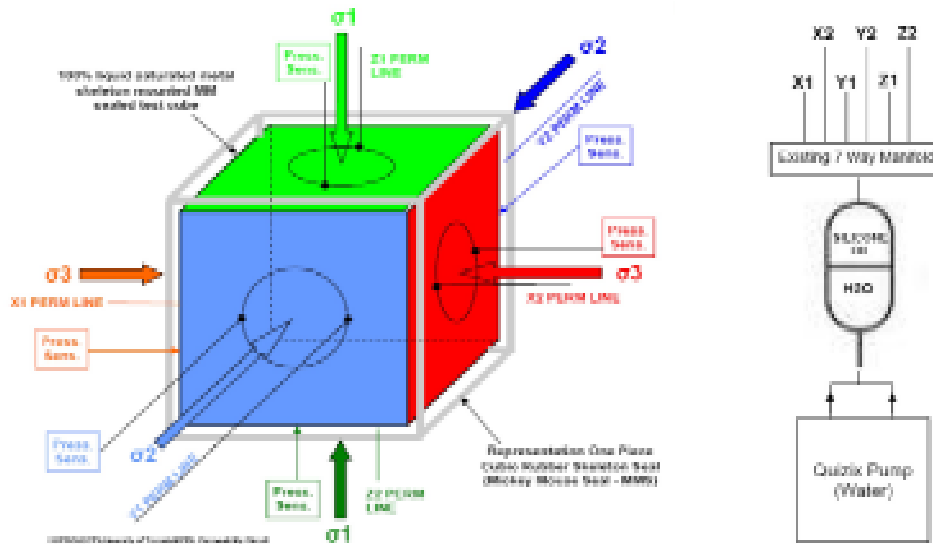


Figure 4 a) shows the cub's color-coded sides corresponding to three principal stress directions and b) shows the required system to activate flexible membrane sealing of 12 edges of MM seal which is indicated by the gray line around the cube on the left, designed and drawn by ErgoTech.

3 RESULTS AND DISCUSSION

3.1 True triaxial strength and deformational responses

Fontainebleau sandstone was tested in an advanced geophysical imaging cell under unequal principal stresses. The least and intermediate principal stresses were kept constant at 10 and 20 MPa respectively while maximum principal stress was increased until failure and beyond. The effective stresses for the three principal stress directions were calculated by compensating for the load, pore and seal pressure affecting each of the six loading actuators. Nine LVDTs were used (three for each direction) to calculate the strain during the experiments. Figure 5 shows variation of stress-strain curves as a function of major principal stress. The stress-strain curves along all three axes show an initial plasticity due to closure of compliant cracks and pore spaces.

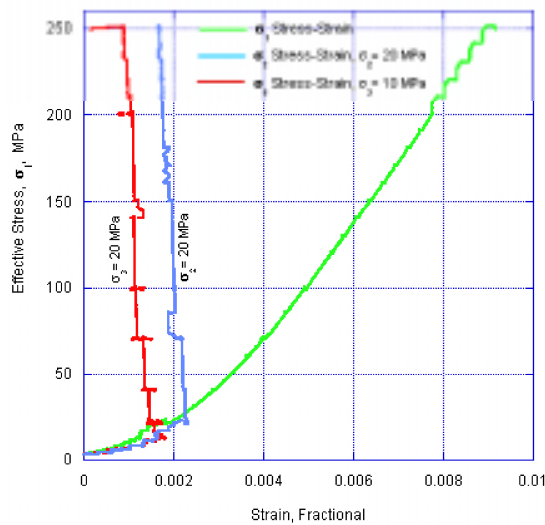


Figure 5. Shows variation of stress versus strain for all three principal stress directions as a function of σ_1 effective stress while σ_2 and σ_3 were kept constant at 10 and 20 MPa of effective stress.

The stress-strain curve measured along σ_1 axis shows linear elastic behavior between 50-100 MPa of axial effective stress. Evolution of the stress-strain curve for σ_1 does not show the classic elasto-plastic type behavior prior to failure as observed with cylindrical specimens in conventional type triaxial experiments. This could be related to the shape of the specimen which is cubic in nature and globally stressed by the stainless steel noncompliant loading platens on all six faces. On the other hand evolution of acoustic emission activity and ultrasonic wave velocity measurements show that the specimen experienced initial stages of failure when σ_1 reached a value of ~ 110 -120 MPa, deforming by about 0.5% in σ_1 direction. The respective deformation in the σ_2 and σ_3 axes at the initial stages of loading shows strain values of 0.18% and 0.22%. However, these values have been further reduced which can be related to the volumetric deformation of the specimen as a function of σ_1 stress increments. The specimen was loaded upto 250 MPa along σ_1 while keeping σ_2 and σ_3 at 20 and 10 MPa respectively. Next, σ_3 was reduced to 5 MPa to cause further damage on the specimen while monitoring the AE and seismic velocities along all three axes.

3.2 Evolution of 3D ultrasonic wave velocities with true triaxial stresses

Using an ASC integrated pulser/amplifier system software, the ultrasonic wave velocity survey measured compressional (V_p) and two shear wave velocities (V_{S1} and V_{S2}) along all three principal stress directions at various stages of σ_1 loading. Figures 6a and 6b show variations of V_p and V_{S1} along all three directions as a function of σ_1 . Figures 7a and 7b show the same variations in combination with the stress-strain curves. V_p as a function of initial hydrostatic stress increases up to 10 MPa and shows an increase from 4.8 km/s to 5.2 km/s. Next, σ_2 and σ_1 were increased simultaneously up to 20 MPa and then σ_1 was increased while keeping σ_3 and σ_2 at constant stress levels of 10 and 20 MPa respectively. V_p along σ_3 direction increases up to a value of 5.35 km/s when σ_1 reaches a value of ~ 120 MPa (effective stress) and then declines to 5.1 km/s as σ_1 reaches 250 MPa. It is interpreted that the induced fracture propagation plane is parallel/sub parallel to the major and intermediate principal stress axes. P-waves particle motions in σ_3 direction are orthogonal to the failure plane and therefore show a reduction in velocity after failure. V_p in the σ_2 direction does not show a similar reduction. V_p in the σ_1 direction continuously increases up to 5.75 km/s as σ_1 is increased to 250 MPa of effective stress which is related to the fact that the induced fracture propagation plane and P-waves particle motions are parallel causing little influence on V_p in the σ_1 and σ_2 directions. V_p increases by up to 1 km/s in the σ_1 direction from when the specimen was hydrostatically loaded (Figs 6a & 7a).

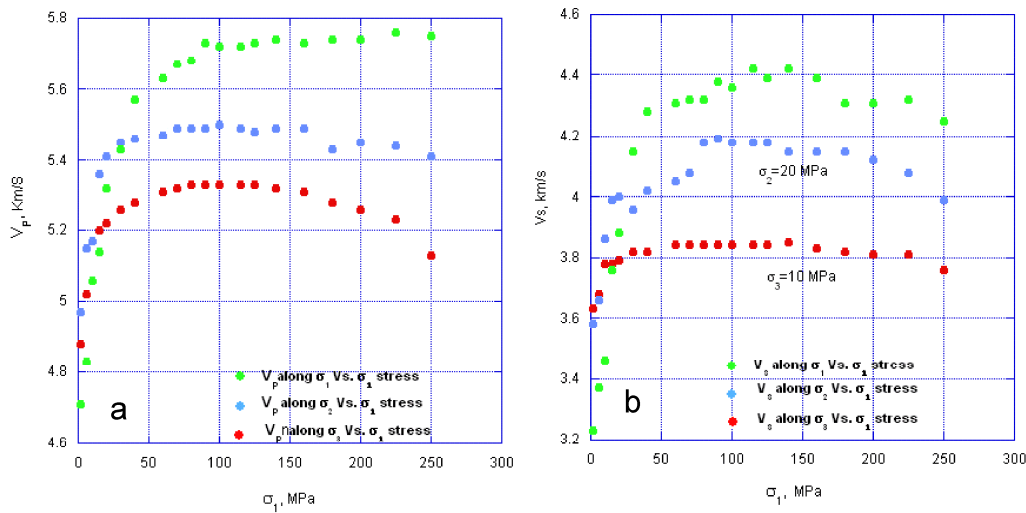


Figure 6 a) depicts variation of V_p along three principal stresses as a function of σ_1 stress while σ_2 and σ_3 was kept at 20 and 10 MPa and b) shows similar variation for V_{S1} .

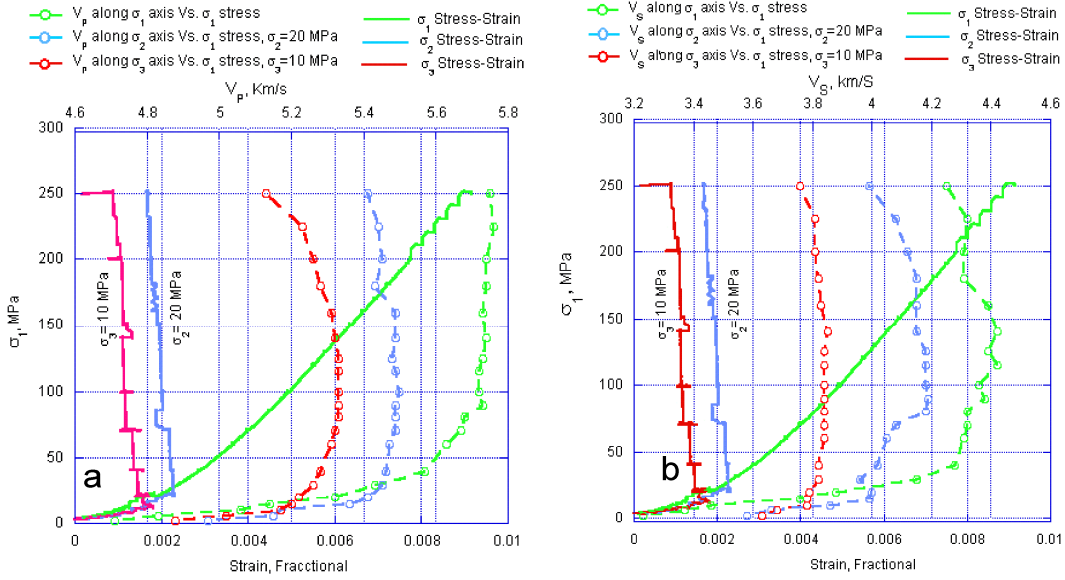


Figure 7 a) variation of stress-strain as a function of σ_1 stress in combination with V_p measured along main principal stress direction while σ_2 and σ_3 was kept at 20 and 10 MPa and b) Variation of the same for V_{S1} .

Variation of shear wave velocity (V_{S1}) as a function of σ_1 measured in all three axes is shown in Figures 6b & 7b. At 10 MPa of hydrostatic stress, V_{S1} measured parallel to all three principal axes shows more or less a similar value of 3.8 km/s which is 1.4 times less than V_p for the same directions. V_{S1} measured along σ_3 did not show any further improvement after failure point and was further reduced as σ_1 was increased to 250 MPa. V_{S1} in the σ_1 and σ_2 directions did decline after peaking at 4.4 and 4.2 km/s respectively around the failure point at 120 MPa. 3D evaluation of directional evolution of the ultrasonic wave velocities shows that stress increments in the σ_1 direction cause closure of microcracks and pore spaces along two horizontal directions as well. This is revealed by the improvement of wave velocities along the two horizontal directions in the specimen prior to failure. Post failure V_{S1} measurements in all the three directions show a decline specifically in the σ_2 and σ_3 directions. Due to space limitations the variation of V_{S2} as a function of axial stress for all three directions is not discussed in the present study.

3.3 Acoustic emission data processing, AE hits and locations

AE source locations were calculated using a Geiger algorithm which used first arrival times selected by an automated routine. Using an appropriate compressional wave velocity (5.5 km/s), source locations were calculated with fewer than 5 arrivals being discarded. A method for estimating the approximate AE location accuracy ($\pm 3-4$ mm) was employed in which source transducers at known locations on the sample surface were pulsed and then located. An AE hit counting system was used to count the total number of AE hits on each sensor (Figs 9a & b). Figure 8a shows the number of AE hits for various sensors and σ_1 as a function of synchronized time. Three main episodes of AE activity are shown in Figure 8a which coincided with the time at which σ_1 was raised to 120, 200 and 250 MPa. Figure 8b shows a magnified section of Figure 8a emphasizing on the first significant episode of AE events recorded during the failure at around 125 MPa of axial stress. It can be seen that propagation of the failure plane takes place sub-parallel to the plane containing σ_1 and σ_2 as expected. Figure 9a shows distribution of acoustic emission source location using only discrete triggered AE events recorded throughout the experiment. Figure 9b shows the result of structural analysis performed on AE events from this episode of AE activity during the experiment. This structural method fits a plane to every permutation of 3 events (events separated < 30 mm) and calculates the pole to the plane.

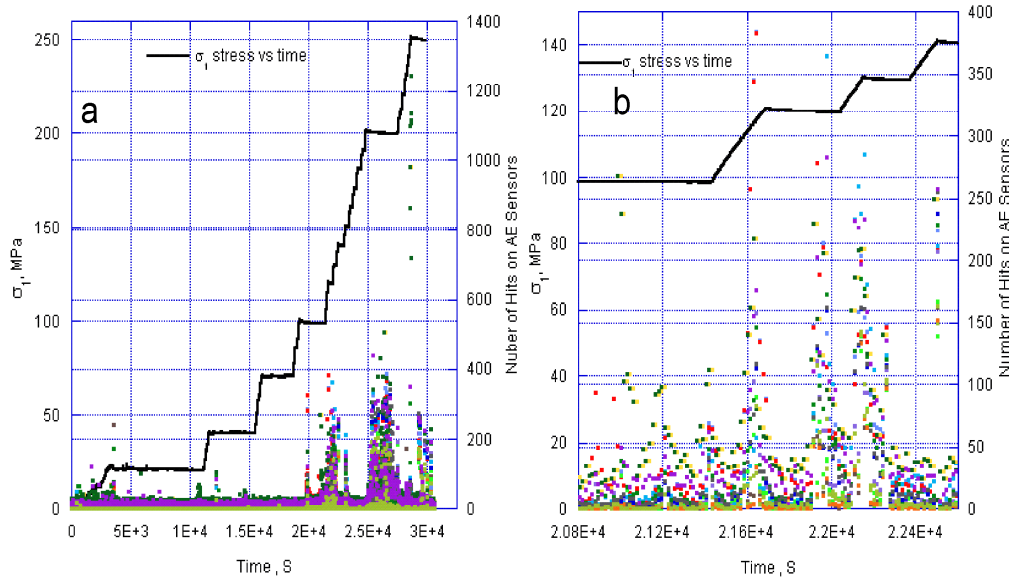


Figure 8 a) shows three main episodes of AE hits in response to σ_1 stress increment versus synchronized time and b) Shows a specific window of AE hits, stress and time during which the first episode of major AE activity around stress level of 105-130 MPa was recorded.

This is displayed in a stereonet with high density corresponding to the pole of the plane following the dominant trend, parallel to σ_1 and σ_2 directions characterized with high to a medium dipping angle and sub-perpendicular to σ_3 direction. The first significant occurrence of AE activity recorded by most of the sensors is related to the time when stress in the σ_1 direction approaches 110-120 MPa at around 5 hours and 50 minutes ($2E+4$ second) after commencement of the experiment. At this time a couple of sensors registered ~ 400 AE events indicating the beginning of fracture initiation and propagation in the specimen. V_p measured perpendicular to σ_3 direction begins to decline at this time. Similar behavior for V_{S1} measured in the σ_1 and σ_2 principal stress directions is observed around 110-120 MPa of axial loading.

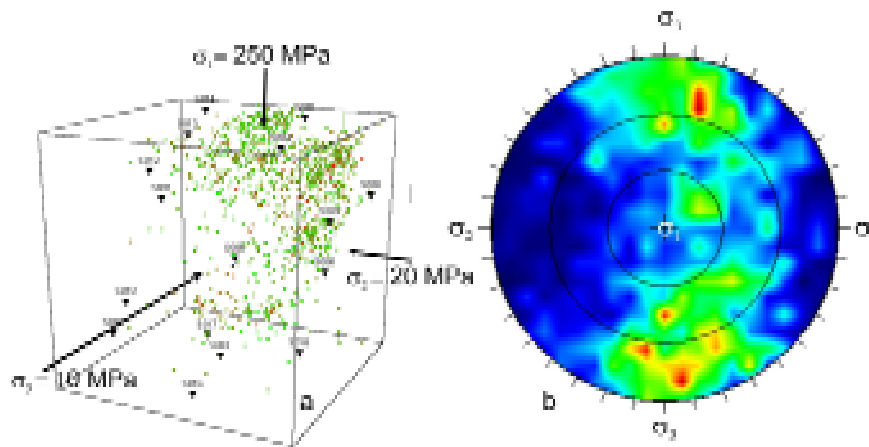


Figure 9 a) source locations for AE induced under true triaxial stress for $\sigma_1 > \sigma_2 > \sigma_3$ when $\sigma_1 = 250$ MPa. The color scale in the figure shows the event magnitude (with brown and red indicating higher magnitude events) and b) Pole density stereograph showing that the orientation of the failure plane being parallel to σ_1 and σ_2 principal stress directions. The red spots represent higher density of poles to the planes intersecting three AE events.

3.4 3D directional permeability of Fontainebleau sandstone

The permeability of Fontainebleau sandstone in all three independent principal stress directions was measured first under 5 and 10 MPa of hydrostatic stress using the steady-state method. Activation of the flexible rubber membrane and MM seal allowed perfect closure of all twelve edges of the cubic sample, providing a unique opportunity to measure the directional permeability of Fontainebleau sandstone for situations where $\sigma_1 = \sigma_2 = \sigma_3$, $\sigma_1 = \sigma_2 > \sigma_3$ and $\sigma_1 > \sigma_2 > \sigma_3$. Figure 10a shows an example of P_p variation recorded by six pore pressure transducers mounted close to the faces of the cube on each loading platen (upstream and downstream sides) for stress levels of $\sigma_3 = 10$, $\sigma_2 = 20$ and $\sigma_1 = 70$ MPa. The pore pressure on the upstream side in the σ_1 direction (Z1 in the Figure 10a) shows a much higher value of P_p , as a function of flow rate, than the other five pore pressures. The downstream side in the σ_1 direction (marked as Z2 side) records the lowest P_p since it is exposed to the atmospheric pressure. The other four faces of the cube measure a P_p value between the aforementioned extreme values. Such a unique P_p distribution is good evidence for proper sealing on all twelve edges of the specimen. Figure 10b shows the variation of permeability for $\sigma_1 = \sigma_2 = \sigma_3$, $\sigma_1 = \sigma_2 > \sigma_3$ and $\sigma_1 > \sigma_2 > \sigma_3$. From Figure 10b, it can be interpreted that K values measured in the σ_2 and σ_3 directions show a significant decrease from $3.3E-15$ m² to $1.55E-15$ and $1.75E-15$ m² respectively as σ_1 is increased to 100 MPa. Variation of K in the σ_1 direction shows a higher decrease to $1.45E-15$ m² due to the closure of pore spaces and the compaction effect. K values measured in all three principal stress directions do not show significant decline after this stage (100-125 MPa of axial stress). K values show a slightly higher decline of up to 1.2 m² in the σ_1 direction during the post failure regime. Such a range of K values for a specimen of Fontainebleau sandstone with ~5% of porosity is in good agreement with the K value reported by Son & Renner (2008). Changes in permeability, V_p and V_{S1} as a function of increasing effective stress in the σ_1 direction, are shown in Figures 11a & b. There is good agreement between the increasing nature of V_p and V_{S1} and the decreasing trend of 3D permeability in all three directions up to the failure point (125 MPa of axial stress). The significant reduction of K values measured in all three directions is caused by closure of pore spaces and microfracture fabrics in the axial direction. This phenomenon has affected the 3D networks and connectivity among pore spaces, making the rock less permeable along the two horizontal directions especially in the σ_2 direction at early stages of differential stress increments. Proportional increment of V_p and V_S seen parallel to the two horizontal planes are good evidence of such compaction and tightness demonstrated by specimen prior to failure. Variation of V_p and permeability as a function of axial stress clearly shows that with further closure of pore spaces in the main principal stress direction during the post failure regime, permeability decreases to its lowest value which is in agreement with increasing V_p in that direction.

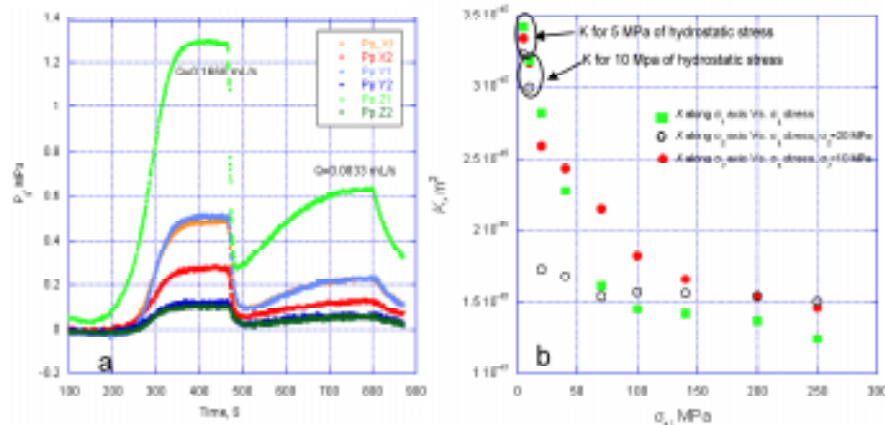


Figure 10 a) variations of six pore pressure values recorded at each loading platen along three principal stress directions, Q values for two stable situations are marked in the graph. Z1-Z2, Y1-Y2 and X1-X2 are platen's name in the σ_1 , σ_2 and σ_3 directions respectively and b) Variation of 3D directional permeability as a function of σ_1 stress while keeping σ_2 and σ_3 at 20 and 30 MPa constant.

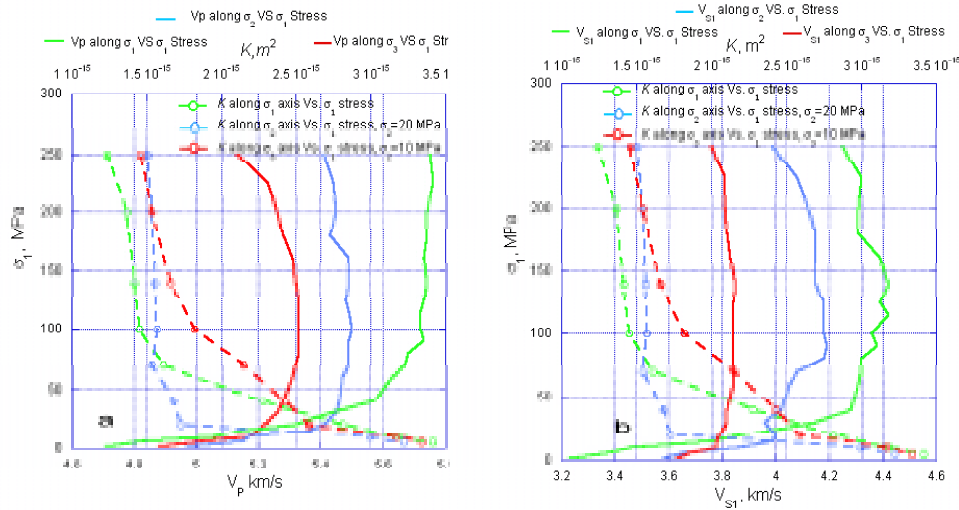


Figure 11 a) shows variation of 3D K and 3D V_p as a function of σ_1 stress increments and b) Shows variation of 3D K and 3D V_{S1} as a function of σ_1 stress increments.

Variation of 3D V_{S1} with 3D permeability also shows a negative correlation up to the failure point. Unlike V_p , V_{S1} measured in the σ_1 direction decreases by 4% during the post failure regime.

3.5 Conclusions

At the RFDF, we have successfully tested a 8 cm³ Fontainebleau sandstone using an advanced true triaxial geophysical imaging cell within a polyaxial MTS frame under $\sigma_1 = \sigma_2 = \sigma_3$, $\sigma_1 = \sigma_2 > \sigma_3$ and $\sigma_1 > \sigma_2 > \sigma_3$ stress states. Our results show a self-consistent relationship among the tested specimen's strength, 3D deformation, 3D wave velocities, acoustic emission and 3D transport properties. Around 110-120 MPa of stress in the σ_1 direction, the creation of preferentially oriented fractures and failure took place which was accompanied by the first significant episode of AE activity. The compressional wave velocity decreased perpendicular to the plane of fracture propagation after failure. Shear wave velocities showed a decline in all three principal stress directions after failure. AE hit counts further climaxed at 200 and 250 MPa of axial stress reflecting more damage caused along the failure planes and V_p measured perpendicular to the failure plane decreased further. AE source location from the first episode of seismic activity delineated the failure plane to be sub-parallel to the major and intermediate principal stress directions and sub-perpendicular to the least principal stress direction. This is in agreement with the 3D compressional wave velocities and the transport properties measured perpendicular to the failure plane. 3D permeability values measured for 5 and 10 MPa of hydrostatic stress shows a decreasing trend with increasing effective stress. On further increments of stress in the σ_1 direction, K values reduced by half in all three directions in spite of the fact that the effective stress in the σ_2 and σ_3 principal stress directions was maintained at 20 and 10 MPa. This indicates that the deformation of the specimen in the σ_1 direction did influence the transport properties in the other two horizontal directions. Above 100 MPa of axial stress the K value was more affected in the axial direction (σ_1) than the other two horizontal directions (σ_2 and σ_3). This study is part of the ongoing research in understanding the effect of the intermediate stress on strength, deformation and transport properties using integrated geophysical imaging methods.

Acknowledgments: We would like to thank Professor Michael King, Dr. Adam Schiffer, Dr. Will Pettitt, Dr Will Flynn, Dr. Xueping Zhao, Dr. Andras Gilicz, Mr. Dylan Roberts, Mr. Mehdi Ghofrani Tabari, Mr. Hamed Ghaffari, and Mr. Sebastian Goodfellow for their valuable contributions and continuous support.

REFERENCES

- Mogi, K. 1966. Some precise measurements of fracture strength of rocks under uniform compressive strength, *Rock Mech. Engng Geol.* 4: 51-55
- Mogi, K. 1971. Fracture and flow of rocks under high triaxial compression, *J. Geophys. Res.* 76: 1255-1269.
- Takahashi, M & Koide, H. 1989. Effect of intermediate principal stress on strength and deformation behaviour of sedimentary rocks at the depth shallower than 2000 m. In *Rock at Great Depth* (eds. V. Maury and D. Fourmaintraux). Vol. 1, 19-26. Rotterdam: Balkema.
- Haimson, B. & Chang, C. 2000. A new true triaxial cell for testing mechanical properties of rocks, and its use to determine rock strength and deformability of Westerly granite. *Int. J. Rock Mech. Min. Sci.* 37: 285-296.
- Descamps, F. & Tshibangu J.P. 2007. Modelling the limiting envelopes of rocks in the octahedral plane. *Oil and Gas Science and Technology-Rev. IFP*, 62(5): 683-694.
- You, M. 2009. True-triaxial strength criteria for rock. *Int. J. Rock Mech. Min. Sci.* 46: 115-12.
- Haimson, B. 2006. True triaxial stresses and the brittle fracture of rock. *Pure Appl. Geophys.* 163:1101-1130.
- Haimson, B., Lin, W., Oki, H., Hung, J.-H. & Song, S.-R. 2010. Integrating borehole-breakout dimensions, strength criteria and leak-off test results, to constrain the state of stress across Chelungpu Fault, Taiwan. *Tectonophysics* 48(2): 65-72.
- King, M.S. 2002. Elastic wave propagation and permeability for rocks with multiple parallel fractures. *Int. J. Rock Mech. Min. Sci.* 39:1033-1043.
- King, M.S., Pettitt, W.S., Haycox, J.R. & Young, R.P. 2011. Acoustic emission associated with the formation of fracture sets in sandstone under polyaxial stress conditions. *Geophysical Prospecting*. doi:10.1111/j.1365-2478.2011.00959.x.
- Cai, M. 2008. Influence of intermediate principal stress on rock fracturing and strength near excavation boundaries - Insight from numerical modeling. *Int. J. Rock Mech. Min. Sci.* 45:763-772.
- Heard, H.C. & Page, L., 1982. Elastic moduli, thermal expansion and inferred permeability of two granites to 350°C and 55 Megapascals, *J. Geophys. Res.*, 87:9349-9348.
- Guéguen, Y. & Dienes, J. 1988. Transport properties of rocks from statistics and percolation. *J. Math. Geol.* 21(1): 131.
- Guéguen, Y., & Schubnel, A. 2003. Elastic wave velocities and permeability in cracked rocks, *Tectonophysics* 370:163-176.
- Reuschle, T. Gbaguidi Haore, S. & Darot, M. 2006. The effect of heating on microstructural evolution of La Peyratte granite deduced from acoustic velocity measurements, *Earth Planet. Sci. Lett.* 243: 692-700.
- Schubnel, A. & Guéguen, Y. 2003. Anisotropy and dispersion in cracked rocks. *J. Geophys. Res.* 108(B2), 2101.
- Schubnel, A. Benson, P.M. Thompson, B.D. Hazzard, J.F. & Young, R.P. 2006. Quantifying damage, saturation and anisotropy in cracked rocks by inverting elastic wave velocities, *Pure Appl. Geophys.* 163:947 – 973.
- Nasseri, M.H.B. Schubnel, A. Benson, P. M. & Young, R. P. 2009. Common evolution of mechanical and transport properties in thermally cracked westerly granite at elevated hydrostatic pressure. *Pure Appl. Geophys.* 166:927-948.
- Song, I. & Renner, J. 2008. Hydromechanical properties of Fontainebleau sandstone: Experimental determination and micromechanical modeling. *J. Geophys. Res.* 113: B09211.
- Haddad, S.C. Worden, R.H. Prior, D.J. & Smalley, P.C. 2006. Quartz cement in the Fontainebleau sandstone, Paris basing, France: Crystallography and implications for mechanisms of cement growth, *J. Sediment Res.* 76: 244-256.
- Fredrich, J.T. Greaves, K.H. & Marin, J.W. 1993. Pore geometry and transport properties of Fontainebleau sandstone. *Int. J. Rock Mech. Min. Sci. Geomech. Abstr.* 30: 691-697.
- Lombos, L. Roberts, D.W. & King, M.S. 2011. Design and development of an integrated true triaxial rock testing system. This volume (see Section 2).